



Characterization of phases in an Fe–Mn–Si–Cr–Ni shape memory alloy processed by different thermomechanical methods



V. Fuster^{a,b}, A.V. Druker^{a,b,*}, A. Baruj^{c,d}, J. Malarría^{a,b}, R. Bolmaro^{a,b}

^a Instituto de Física Rosario (CONICET-UNR), Bv. 27 de Febrero 210 bis, 2000 Rosario, Argentina

^b Facultad de Cs. Ex., Ingeniería y Agrimensura (UNR), Av. Pellegrini 250, 2000 Rosario, Argentina

^c Centro Atómico Bariloche, Comisión Nacional de Energía Atómica (CNEA), Av. Ezequiel Bustillo 9500, 8400 S. C. de Bariloche, Argentina

^d Instituto Balseiro (UNCuyo), Av. Ezequiel Bustillo 9500, 8400 S. C. de Bariloche, Argentina

ARTICLE INFO

Article history:

Received 2 September 2015

Received in revised form 21 September 2015

Accepted 22 September 2015

Available online xxxx

Keywords:

Ferrous shape memory alloys

Microstructure

Phase analysis

Fe₃Ni₃Si₂ type intermetallic

X-ray diffraction

Rietveld refinement/Maud.

ABSTRACT

The presence of second phases in FeMnSi-based systems has been widely discussed in the literature, and also in our previous works. In this manuscript, various specimens of an Fe–15Mn–5Si–9Cr–5Ni wt.% (nominal composition) shape memory alloy were processed by different thermomechanical treatments in order to identify the phases present in each condition. TEM-EDS results indicate that the chemical composition of the second phase we found in all cases is close to 19Mn–xSi–12Cr–5Ni at. %, with x varying between 5 and 11, and Fe balance. This is compatible with a Fe₃Ni₃Si₂ type intermetallic phase. It forms in a temperature range between 600 and 900 °C, independently of the thermomechanical processing and the coexisting phases. Rietveld refinement of X-ray patterns was done using Maud software, and the phase was found to be isostructural to the pi-phase Cr₃Ni₃Si₂ with space group P2₁3 and lattice parameter equal to 0.6227(7) nm. Phase quantification, crystallite size and accumulated microstrain were also computed as a convenient set of variables, necessary for improving refinement quality. Relevant microstructural information, i.e. stacking fault and twinning probabilities, along with dislocation density, were calculated for austenite, the matrix phase, contributing to the reliability of the determination of the crystallographic characteristics of the second phase.

© 2015 Elsevier Inc. All rights reserved.

1. Introduction

Fe–Mn–Si-based shape memory alloys (SMAs) have been extensively investigated during the last three decades [1,2]. Their shape memory effect (SME) is due to a stress-induced γ (austenite, FCC) \leftrightarrow ε (martensite, HCP) martensitic transformation that reverses when the material is heated above the A_f temperature. For the best recovery of the original shape the plastic deformation accompanying martensitic transformation must be negligible, and the $\varepsilon \rightarrow \gamma$ reverse transformation has to occur along the same crystallographic path followed during the direct transformation. The alloy's stacking fault energy (SFE), the microstructure and texture of the austenitic phase are the main parameters that affect the SME. Previous works have demonstrated that a favourable defect structure, i.e. a high density of stacking faults and an appropriate balance of dislocations, may be controlled by applying thermomechanical treatments to a material with the appropriate chemical composition [3–6].

Sade et al. [7] summarized literature indicating that Fe–Mn–Si-based SMAs usually contain between 15 and 30 wt.% Mn in order to stabilize the FCC \rightarrow HCP transformation. A lower Mn content decreases the ε -martensite stability while that of the α' -martensite (BCC) increases. In

fact, if the amount of Mn is lowered, the increase in M_s temperature needs to be compensated by the addition of 4–5 wt.% Ni. Another component is Si, usually up to 6 wt.% to control the SFE and the austenite antiferromagnetic ordering temperature (Néel temperature, T_N). The addition of Cr, generally between 5 and 9 wt.%, improves the material's corrosion resistance. But when the Cr quantities are above 7 wt.%, the brittle Fe–Cr sigma phase (σ_{Fe-Cr}) can form [8]. In such cases, Ni is added to prevent σ -phase formation, in a similar way as for stainless steels [9].

The Fe–Mn–Si–Cr–Ni SMAs system provides a way for producing a training free Fe–Mn–Si-based alloy with high recovery strain. In addition, it can be expected that an even higher recovery strain can be developed in the cast condition through optimization of alloy compositions, casting parameters and heat-treatment techniques [10,11].

These SMA alloys contain elements that competitively stabilize the FCC and BCC phases and have a tendency to form different solid solutions and compounds. Many authors have reported the presence of phases that affect properties or reduce the amount of austenite available to transform to ε -martensite. We will briefly summarize their results in what follows.

Lin et al. [12] investigated the formation of a grain-boundary phase in the Fe–30Mn–6Si–5Cr SMA during annealing at temperatures ranging from 600 °C to 750 °C, which forms in a large amount at 700 °C. This phase exhibited an ordered BCC structure with a lattice parameter

* Corresponding author at: Instituto de Física Rosario (CONICET-UNR), Bv. 27 de Febrero 210 bis, 2000 Rosario, Argentina.

E-mail address: druker@ifir-conicet.gov.ar (A.V. Druker).

of about 0.8798 nm, and had a similar chemical composition to that of the matrix. The SME and tensile properties of the alloy continuously degraded with increasing amounts of grain-boundary phase.

Maji et al. [13] studied the microstructure and phase stability of an Fe–15Mn–7Si–9Cr–5Ni stainless SMA in the temperature range of 600 °C to 1200 °C. They found an austenite single-phase field in the temperature range of 1000 °C to 1100 °C and a three-phase field, consisting of austenite, δ -ferrite, and the (Fe, Mn)₃Si intermetallic phase, above 1100 °C. Within the temperature range of 700 °C to 1000 °C, a two-phase field consisting of austenite and a Fe₅Ni₃Si₂ type intermetallic phase exists, and below 700 °C, a single austenite phase field exists. Apart from these equilibrium phases, the austenite grains show the presence of athermal ε -martensite. The athermal α' -martensite has also been observed for the first time in this kind of alloys and is produced through the $\gamma \rightarrow \varepsilon \rightarrow \alpha'$ transformation sequence.

Stanford et al. [14] investigated the stability of austenite in a number of Fe–Mn–Si-based SMAs. They found that grain-boundary BCC structure precipitates formed over a wide range of alloy compositions and heat-treatment temperatures. This grain-boundary precipitates have been identified as the chi (χ) phase. Although up to 3 vol.% of the grain-boundary precipitates were generated by isothermal ageing in the range of 500–800 °C, it was found not to markedly affect the mechanical properties or the shape memory behaviour. Afterwards, Stanford et al. [15] examined the interplay of composition, stacking fault probability (SFP) and T_N on the SME for a range of Fe–Mn–Si-based SMAs. The SFP (inversely proportional to stacking fault energy) showed little correlation to the SME for the range of examined alloy compositions. Furthermore, the T_N was not found to have a significant effect on the SME. However, the addition of interstitial elements was found to markedly decrease the SME. TEM showed that there were no carbides formed in an alloy with 0.3 wt.% C because a high Si content probably inhibits carbide formation during thermomechanical processing.

Kirindi et al. [16,17] analysed some physical and mechanical properties of martensitic transformation in an Fe–12.5Mn–5.5Si–9Cr–3.5Ni (wt.%) SMA. Compressive deformation at room temperature, when applied to the ε (HCP) phase within the austenite phase, caused the formation of α' (BCC) martensite crystals at the intersection of prior ε -martensite plates. Newly formed ε -martensite plates were also observed.

Wen et al. [18] focused on the microstructures and shape recovery of a cast Fe–18Mn–5.5Si–9.5Cr–4Ni alloy. They attained lathy ferrite which subdivide the austenitic grains and resulted in the formation of stress-induced martensite bands in a domain-specific manner, which generated a high degree of shape recovery. In other words, in one domain only one group or one dominant group of ε -martensite bands is induced. Some σ -phase precipitated inside the ferrite. This was explained by the high Si content, which can shift the σ -phase region to that of low Cr content and accelerate the precipitation of this phase. When the Si content reaches 2.5 wt.%, the σ -phase region expands to Cr contents as low as 10 wt.% [19]. Wen et al. also found results indicating that ferrite with lathy morphology could improve the SME of Fe–Mn–Si alloys, while ferrite with island morphology could not. The reason for this effect may be that the latter cannot subdivide austenitic grains as efficiently as lathy ferrite.

To improve wear resistance, Bu et al. [20] studied the effects of ageing at 850 °C — with and without pre-deformation at room temperature — on the precipitation of second-phase particles in an Fe–14.51Mn–6.02Si–9.10Cr–5.06Ni–1.49Ti–0.16C SMA. They found that after solution treatment at 1100 °C there were massive amounts of ferrite in the austenitic grain boundaries. A subsequent ageing at 850 °C promoted the precipitation of some σ particles inside the ferrite phase and few particles within the austenite grains. In addition to the precipitates in the massive ferrite phase, numerous Cr₂₃C₆ precipitates were found inside the austenite grains after a solution treatment at 1100 °C for 40 min, followed by 10% tensile deformation at room

temperature, and subsequent ageing at 850 °C for 30 min. EDS analysis revealed that some particles were TiC and other rod-like particles were rich in Cr, Mn and Si.

Lin et al. [21] added a little amount of rhenium (0.05–0.3 wt.%) to Fe–30Mn–6Si–5Cr alloys to improve the SME. They analysed the martensitic transformation, crystal structure, and ageing precipitates. They state that optimization of shape-memory performance can be achieved through combining pre-straining, ageing, and shape-memory training. The ageing precipitates could be observed in both the grain boundaries and within the grains. The alloys with and without Re, were aged at 700 °C for 2 h. From selected area diffraction patterns (SADP), the ageing precipitates were identified as χ -phase, with BCC structure and a lattice constant close to 0.89 nm. According to Yang et al. [22], the structure of the χ -phase is an A12 (α -Mn) type with 58 atoms in the unit cell. The composition of χ -phase is close to the matrix, but apparently with less Fe atoms and more of the other alloying elements.

Peng et al. [11] investigated the microstructure and solidification modes of cast Fe–(13–27)Mn–5.5Si–8.5Cr–5Ni SMAs, to clarify if Mn was an austenite former during solidification. Some second-phase particles appeared in the 15–27Mn alloys. In the case of 15–21Mn alloys, EDS measurements showed that their chemical compositions were compatible with the σ -phase composition. However, the character of those particles was not clear in the 23Mn–27Mn alloys. Another island-like phase was also found in 23–27Mn alloys. The EDS results on 25Mn and 27Mn alloys indicated that its Mn and Ni contents were markedly higher than those of austenite. By SADP they determined that it was the χ -phase, which is in agreement with the results of Stanford et al. [14]. In the cast Fe–Mn–Si–Cr–Ni alloys, the χ -phase precipitated during the solidification process between the ferrite dendrites by a process which is still unclear.

In a previous paper [23], we showed results on Fe–15Mn–5Si–9Cr–5Ni ribbons produced by the melt-spinning technique, and analysed the ribbon's microstructure and phase stability, evaluating their shape memory properties. The compositional Cr_{eq}/Ni_{eq} ratio, approximately 1.7, predicts that the solidification sequence should be Liquidus \rightarrow L + $\delta \rightarrow$ L + δ + $\gamma \rightarrow$ γ + δ [10]. Thus, the cooling rate determines whether ferrite, ferrite + austenite, or only austenite is present at room temperature, as demonstrated in different melt-spun ribbons. Other than these phases, X-ray diffraction showed less intense peaks indicating the existence of precipitated phases in certain manufacturing conditions. The analysis of the diffractograms suggested that the precipitates corresponded to a Fe₅Ni₃Si₂ type compound, in agreement with Maji et al. [13]. Microscopic analysis showed that the precipitates were distributed within the grains and in the boundaries. More recently, we presented a manufacturing process for shaft and pipe couplings of Fe–Mn–Si–Ni–Cr SMAs [24]. We addressed the formability and weldability of sheets rolled at 800 °C followed by annealing at 650 °C, and investigated how welding affects the mechanical and shape memory properties. X-ray patterns of the base alloy showed the predominant presence of austenite and low-intensity peaks corresponding to a second phase in the welded section. Both phases were clearly recognizable in high-magnification OM images. According to XRD analysis, we believe these peaks to be characteristic of a Fe₅Ni₃Si₂ precipitate. However, given the doubts other authors refer in the literature, we left the door open for further analysis.

Due to the wide interest in this issue, this article is devoted to analyse the different phases found in an Fe–15Mn–5Si–9Cr–5Ni SMA. For this purpose we subjected specimens to various thermomechanical treatments, which generated appreciable amounts of a secondary phase, hereinafter referred to as *precipitated particle phase* (PP-phase).

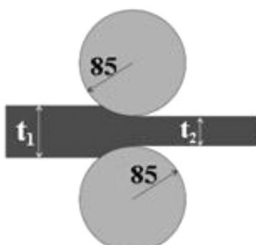
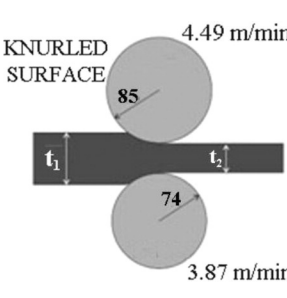
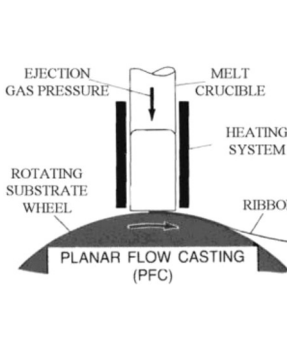
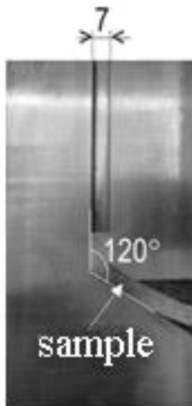
2. Materials and Methods

The Fe–15Mn–5Si–9Cr–5Ni wt.% (nominal composition) alloy was prepared in an induction furnace operating at 10 KHz and 30 KW.

Commercial raw material was melted in high purity alumina crucibles under a protective argon atmosphere and cast into rectangular sand moulds, providing a shape suitable for rolling. The ingots were homogenized at 1150 °C for 3 h to eliminate segregation defects. Then, sections of the cast blocks were processed by the methods described in Table 1.

Samples for microstructural analysis were mechanically and electrolytically polished in an 80–20 (vol.%) acetic–perchloric acid solution at room temperature and 27 V. Microstructural analysis were performed using a PME3 Olympus optical microscope equipped with a NIC device, and a Philips CM200 transmission electron microscope (TEM) operating at 200 kV with an ultra-twin objective lens. TEM specimens were electropolished using the double-jet technique in a 90–10 (vol.%) a-

Table 1
Different processing methods applied to the alloy.

	<p>CR: Conventional rolling in two stages with a 10% rolling reduction per pass. Firstly, rolling at 1000 °C (temperature of the furnace) with a reduction from 10 to 1.95 mm in successive passes; and secondly, rolling at 800 °C to 1 mm final thickness. Finally, the sheets were annealed at 650 °C for 30 min.</p>
	<p>AR: Asymmetric rolling in two stages. Firstly, rolling at 1000 °C with a 10% reduction per pass, from 10 to 5.4 mm thickness; and secondly a 0.05 mm reduction per pass to 3.19 mm final thickness for maximization of the shear stresses. Finally, the asymmetric rolled sheets were annealed at 650 °C for 30 min.</p>
	<p>P6: Rapid solidification. Ribbons approximately 0.03 mm thick and 10 mm wide were produced by a melt-spinning technique [23] and then encapsulated in quartz glass in Ar atmosphere for annealing at 600 °C for 60 min. At first, the starting material was cut into small pieces that were induction-coil melted in a quartz crucible, and ejected by argon pressure onto a Cu-(Co, Be) rotating substrate wheel. The wheel speed, pressure, alloy's melt temperature, wheel temperature and crucible-substrate gap, were 20 m·s⁻¹, 200 mbar, 1450 °C, 25 °C and 0.2 mm, respectively.</p>
	<p>ECAP: Samples from Equal-Channel Angular Pressing experienced finite shear deformation. A bar with a 7 × 7 mm² cross section was passed through two butted channels joined at an angle of 120°, at a speed of 5 mm min⁻¹ and a temperature of 250 °C. Subsequently, samples of the deformed material were heat treated at 800, 900 and 1000 °C for 30 min, and the samples were denominated E8, E9 and E10, respectively. Specimens from each batch were compressed to a strain of 3.8%.</p>

temperature. X-ray diffraction patterns and pole figures were measured using Cu-K α_1 /K α_2 lines in a Philips X-pert pro MPD goniometer at 40 kV and 30 mA. The scans were carried out from 30 to 85°, in 0.02° 2 θ steps, and 10 s collecting time per step. Texture was measured collecting austenite γ -phase (111), (110) and (100) pole figures ranging from 0 to 85° in ϕ , and 0 to 360° in φ with 5° angular steps and 1 s collecting time per step, as described in [25]. The instrumental standard chosen to account for instrumental broadening was NIST LaB₆ [26]. X-ray characterization of each sample was performed by Rietveld refinement [27] of the corresponding patterns, using the Java based software Maud (Materials Analysis using Diffraction) version 2.55 released April 30, 2015 [28,29]. This programme allows for incorporation of microstructural and full texture, or preferred orientation, analysis into the traditional refinement [30–33]. The martensitic transformation was induced in an Instron 3362 universal testing machine.

3. X-ray analysis

The X-ray study comprises a series of iterations in order to minimize the root mean square errors of certain parameters associated with sample or instrumental variables [34]. Since Maud allows separating instrumental and sample contributions to peak width, each refinement takes into account the instrumental parameter file obtained by refinement of the LaB₆ X-ray pattern.

Thermomechanical treatments introduce substantial microstructural changes, due to defect multiplication and migration, activation of certain slip systems, etc. As a consequence, grains reorientate favourably and/or recrystallize at high temperature in a manner consistent with the crystallography of the present phases, as well as with the applied tensile, compressive, shear or torsion stress direction. The preferred orientation of grains or texture must be taken into account during the refinement. It is modelled by the Orientation Distribution Function (ODF), which is a three-dimensional statistical function representing the probability of finding crystallites (hkl) with a certain orientation relative to sample coordinates.

This alloy typically develops low-intensity texture, as documented previously [25,35]. We used the WIMV method, incorporated in Maud, to compute the ODF from experimental austenite (111), (200) and (220) pole figures, which coincided with our previous measurements [25]. However, the relative intensities of X-ray reflections were not adequately fitted with this method, possibly because the reduced number of pole figures did not provide sufficient statistical data to reconstruct the ODF. This is a limitation of these types of materials, where the major phase is of high symmetry and few reflections with a low (hkl) index are found. More realistic pole figures can be acquired with synchrotron measurements, but this is beyond the scope of the present work. We alternatively modelled the ODF with the March–Dollase method and with the Roe and Bunge method, i.e. as a series of spherical harmonics [36]. Better agreement between the experimental and reconstructed pole figures was observed using the latter model. On the other hand, the refinement was rather unstable and gave physically meaningless results when applying the arbitrary texture option of the programme. Therefore, and considering that this work is not devoted to texture analysis, we modelled each phase ODF with a harmonic expansion. According to Lutterotti et al. [37], this method is useful for weak texture and high crystal-symmetry phases, which is the case of our material. We believe that the crystallographic and microstructural information obtained by this method is sufficient for comparison purposes.

The crystallite size $\langle D_{eff} \rangle$ and accumulated microstrain $\langle \varepsilon_{hh}^2 \rangle^{1/2}$ due to perfect dislocations were obtained using the Popa model [38], which is suitable for anisotropic properties, i.e. reflections of the same phase with different Miller indices broaden in different ways. In this work we were able to refine only one coefficient of the expansion series. This suggests that the crystallite is almost spherical and the strain tensor is approximately isotropic.

Maud analysis also permits quantitative estimation of crystallographic defects such as stacking faults, twinning and dislocation density [31]. This is especially interesting since the most accepted mechanism for the $\gamma \rightarrow \epsilon$ transformation is the motion of Shockley partial dislocations on every second (111) austenite plane, generating a stacking fault through (111)[112] slip. Warren's model [39] describes three types of alloy defects in terms of refinable probabilities: intrinsic stacking faults (α'), extrinsic stacking faults (α'') and twinning (β). They contribute to peak shift, anisotropic broadening and asymmetry [39–41]. In short, intrinsic stacking faults occur when mechanical deformation induces (111) plane slip, modifying the normal γ -FCC sequence ABCABC into a new ABCA(C)ABC stacking, where four planes pile up in the sequence typical of the HCP structure. Twinning can arise during crystal growth, when two consecutive (111) planes slip in the same way so that the new stacking sequence becomes ABC(A)CBA. In this case, the fault plane (A) is the boundary between two parts of the crystal which are the mirror image of each other. An extrinsic stacking fault is the minimum twin that involves three ABC planes where the new sequence becomes ABC(ACB)CA.

Faults shift and broaden diffraction peaks differently, depending on the (hkl) family of planes and the individual components which are truly affected by such defects. Hence, each reflection can be shifted towards a higher or lower angle in the measured peak displacement $\Delta(2\theta)^\circ$, which is expressed as in Eq. (1).

$$\Delta(2\theta)^\circ = \frac{90\sqrt{3}(\alpha' - \alpha'') \tan\theta}{\pi^2 h_0^2 (u + b)} \sum_b (\pm L_0) \quad (1)$$

where $h_0 = (h^2 + k^2 + l^2)^{1/2}$, $L_0 = h + k + l$, and b and u are the number of peak components broadened and unbroadened by faults, respectively. The refinable parameters in Maud are α' and α'' .

The effective crystallite size $\langle D_{eff} \rangle$ obtained from the refinement is the average of the coherent domains, D , normal to the reflecting planes (hkl) (Eq. (2)). The effective size is affected by crystal defects because dislocation arrays and stacking faults can subdivide the original grains into smaller coherent crystalline domains which scatter incoherently with respect to one another [39]. This size is calculated in Maud as:

$$\frac{1}{D_{eff}} = \frac{1}{D} + \frac{[1.5(\alpha' + \alpha'') + \beta]}{a h_0^2 (u + b)} \sum_b |L_0| \quad (2)$$

Eq. (2) is based on the Warren–Averbach method, where a is the cell parameter and the term $[1.5(\alpha' + \alpha'') + \beta]$ is the expression of the compound fault probability, in the case of FCC and BCC structures. It changes into $[3(\alpha' + \alpha'') + k\beta]$ (where k is an integer) for HCP crystals. β is another refinable parameter.

The peak asymmetry is obtained measuring the value of the intensity on either side of the peak at two positions which are equidistant from the peak centre (y_1 and y_2), and is mainly related to the development of twin faults. The mathematical expression for asymmetry is:

$$y_2 - y_1 = \frac{2Ab(4.5\alpha'' + \beta)}{\sqrt{3}\pi(u + b)} (\pm) \frac{L_0}{|L_0|} \frac{1}{c_2 x_2} \quad (3)$$

where the coefficient c_2 in Eq. (3) depends on the peak $2\theta_0$ position (see Eq. (4)).

$$c_2 = 1 + \left\{ \frac{\lambda}{4\pi D_{eff} [\sin(\theta_0 + x_2) - \sin\theta_0]} \right\}^2 \quad (4)$$

According to Williamson et al. [40], the average dislocation density ρ_{av} is calculated from ρ_D (due to crystallite size) and ρ_S (due to

microstrain), as in Eq. (5):

$$\rho_{av} = (\rho_D \rho_S)^{1/2} \quad (5)$$

where $\rho_D = 3/D_{eff}^2$ and $\rho_S = (K \langle e^2_{hh} \rangle)/b^2$. Assuming a Gaussian microstrain distribution, $K = 16.6$ for an FCC structure and $K = 14.4$ for a BCC crystal. b represents the dislocation Burger's vector, which is $a/\sqrt{2}$ in the [110] direction in an FCC structure, whereas it equals $a\sqrt{3}/2$ in the [111] direction in BCC crystals.

The goodness of fit is determined as in Eq. (6):

$$GoF = \frac{R_{wp}}{R_p} \quad (6)$$

where R_{wp} is the weighted residual error and R_p is the expected error. Convergence is reached when GoF approaches 1. It is a measurement of the reliability of the whole refinement.

4. Results and discussion

4.1. Microstructural characterization and chemical composition

Fig. 1 shows OM images of the microstructure of samples taken from the different procedures. Fig. 1a corresponds to a conventionally rolled sheet where austenite grains have the lightest contrast and a second phase is recognized by the light grey colour. Vickers indentations vary greatly, which indicates an important hardness difference between the two phases. The measured values were HV 315 and 990, respectively [24]. Fig. 1b corresponds to an ECAP sample annealed at 800 °C for 30 min, and then compressed to 3.8% strain to activate the martensitic transformation. However, the great majority of the ϵ -martensite plates formed during the ECAP deformation. Also, precipitates were found in this material. Fig. 1c shows an ECAP sample after annealing at 900 °C for 30 min. This treatment activated the recrystallization of deformed austenite grains and the precipitation of the secondary PP-phase, which is mainly located at grain boundaries but also within the grains. Vilella's reagent was used to outline the second-phase particles. Finally, Fig. 1d is the OM image of an ECAP sample annealed at 1000 °C for 30 min and then compressed to 3.8% strain. The structure is stress-induced ϵ -martensite in an austenitic matrix.

The TEM images in Fig. 2 correspond to specimens taken from the P6 ribbon. The precipitates are distributed within the austenitic grains and some of them are located near the foil edge. The chemical composition of the precipitates labelled 1 and 2 in Fig. 2a, and others similarly located in the ECAP specimen annealed at 800 °C and 3.8% compressed, was measured using TEM-EDS. The values are reliable due to the absence of contributions from the matrix. Table 2 summarizes the chemical composition of both phases in atomic percentage (as hereinafter).

The precipitates contain all the elements present in the alloy. The measured amount of alloying elements in the precipitates is higher at the expense of iron content, which appears reduced relative to the matrix.

On the other hand, around the precipitate observed in Fig. 2b, the elastic distortion contrast shows that there is (some) coherence with the matrix, although a dislocation is clearly present. The precipitate is nearly circular, but still shows some faceting. Furthermore, there is elastic contrast within the precipitate. The samples were analysed using selected area diffraction (SAD). In this ribbon sample, with a zone axis $[\bar{1}12]_{FCC}$, precipitates can be recognized by the presence of extra spots in the SAD image inset in Fig. 2b. Evidence of the precipitates is the presence of satellites, resulting from elastic deformation associated with the coherence, and also the existence of extra spots. These extra spots appear in the middle between the transmitted beam and diffracted beams corresponding to austenitic {131} diffracting planes. This configuration indicates that there is a superstructure that repeats every two (131) planes. To identify the precipitate's crystallographic structure,

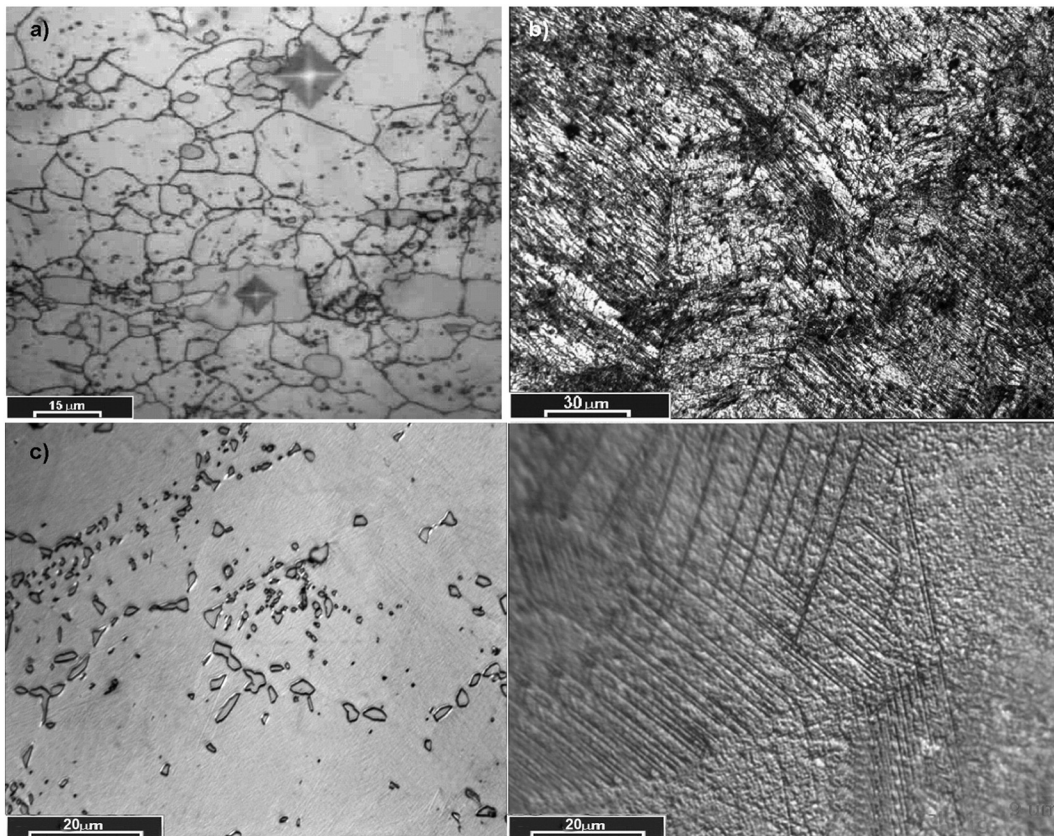


Fig. 1. OM images corresponding to: (a) The conventionally rolled material showing austenite (the white constituent) and a second phase (light grey). (b) The ECAP material, after annealing at 800 °C and 3.8% compression. Many ϵ -martensite plates are observed. (c) The ECAP material, after annealing at 900 °C. The structure is composed of precipitates, mainly located at grain boundaries and in the austenitic matrix. (d) The ECAP material, after annealing at 1000 °C and 3.8% compression. Plates of ϵ -martensite lie in the austenite grains (NIC image).

we compared the extra spots with the standard spot diffraction patterns reported in the literature [42]. We found agreement with the standard pattern corresponding to the $P2_13$ structure. The arrows, in Fig. 2c with a zone axis $[111]_{P213}$, indicate the spots due to the precipitate. Fig. 2d is a dark field (DF) image taken using the spot indexed as $\bar{1}10$.

4.2. X-ray diffraction patterns

The X-ray diffractograms of the samples described in Section 3 are shown in Fig. 3. Each phase is identified by its traditional Greek symbol, followed by the Miller indices (hkl) of the corresponding set of planes satisfying the diffraction condition. The PP-phase is identified by the ∇ symbol.

The specimens under analysis are mainly austenitic. The crystal structure of γ -austenite is FCC, Cu-type, Pearson symbol cF4, space group $Fm\bar{3}m$ #225 [43]. For the Rietveld analysis the atomic occupation of crystallographic sites was set consistent with the alloy chemical composition depicted in Table 2. The cell parameter, obtained by averaging over our refinement results, is 0.3615 nm (see Table 3). This is slightly larger than that of pure γ -Fe (0.36 nm), as expected taking into account that the current austenite is a substitutional solid solution of Mn, Cr, Ni and Si in Fe.

Other common phases found in this system are δ -ferrite in the P6 sample [23] and stress-induced ϵ -martensite observed in E8 and E9. The δ -ferrite phase crystallizes in a BCC structure, W-type, cI2, $Im\bar{3}m$ #229 [43]. The lattice constant is 0.2876 nm, obtained through Rietveld refinement. On the other hand, ϵ -martensite exhibits hexagonal symmetry HCP, Mg-type, hP2, $P6_3/mmc$ #194 [43], with atomic constants $a = 0.2555$ nm and $c = 0.4145$ nm. Once more, our measured cell parameters differ somehow from those of pure Fe: $a = 0.2932$ nm in δ -

Fe, and $a = 0.2473$ nm and $c = 0.3962$ nm in ϵ -Fe. The metallic atoms in the solid solution have different radii and the unit cell expands or contracts when the substitutional atoms occupy the corresponding crystal sites. Still, the length variations are negligible in view of the proximity of the alloying elements in the periodic table: all of them are 3d transition metals.

In addition, according to the microstructural observations and the X-ray diffraction measurements, all the samples have a significant proportion of a unique PP-phase. We specifically analysed these cases to obtain enough information about its properties. Three main PP-phase X-ray reflections are readily observed in the diffractograms of Fig. 3, located at $2\theta = 46.292^\circ$, $2\theta = 48.694^\circ$ and $2\theta = 55.433^\circ$. Minor reflections are also indicated. The 2θ position of these reflections points to a cubic structure of lower symmetry than FCC or BCC crystals.

Another interesting fact is that the PP-phase forms under variable experimental conditions, as also claimed by other researchers. We found it in the CR and AR rolled samples annealed at 650 °C, in the P6 ribbon after annealing at 600 °C, and in the ECAP samples treated at 800 and 900 °C. In a third ECAP specimen, further annealed at 1000 °C and 3.8% compressed (E10), the PP-phase is not found (see Fig. 4). Probably the PP-phase dissolves into the austenitic matrix at such high temperature. This could be in line with the results of Maji et al. [13]. They claim that austenite coexists with an intermetallic phase of the type $Fe_5Ni_3Si_2$, termed as τ -phase by Ackerbauer et al. [44], which form in the temperature range of 700 °C to 1000 °C. That intermetallic is isostructural to the cubic π -phase $Cr_3Ni_5Si_2$ ICSD N° 43384 [45], described as Au_4Al -type, cP20, $P2_13$ #198 [43].

Additionally, the currently identified PP-phase appears in each specimen independently of the presence of other phases. From TEM micrographs presented in Section 4.1, and in previous works, we have found

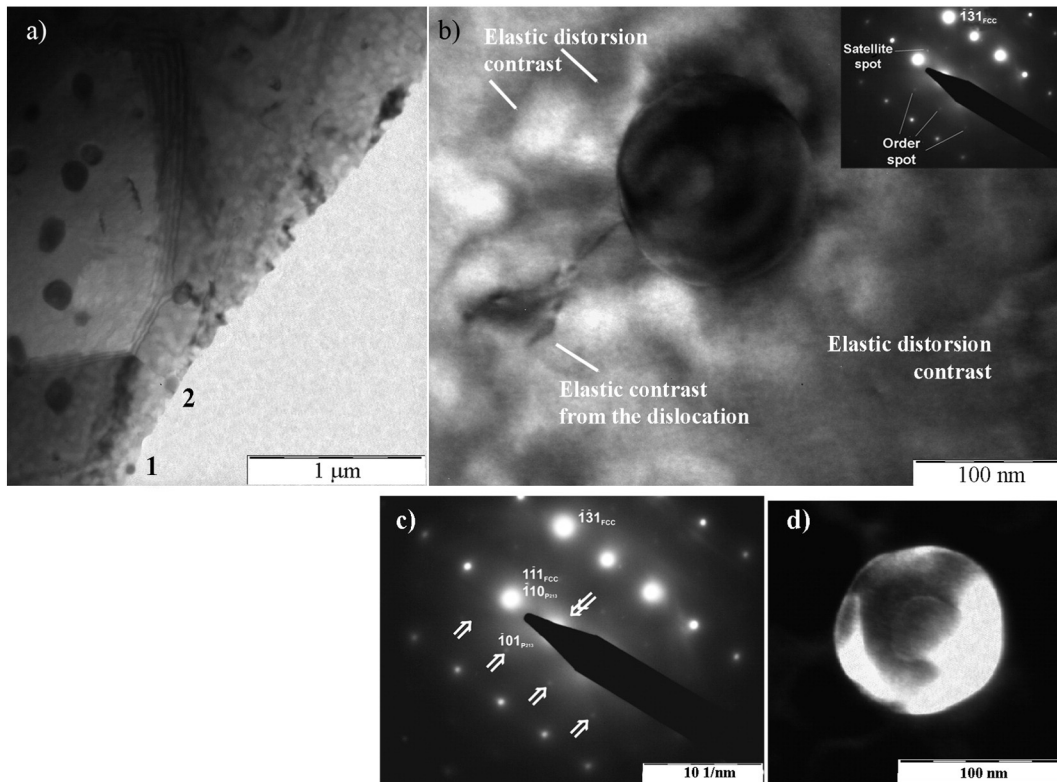


Fig. 2. (a) A TEM micrograph showing precipitates in the austenitic matrix of the ribbon specimens; (b) a high-magnification image showing elastic distortion contrast close to one precipitate. The inset shows the selected area diffraction (SAD) pattern. (c) The pattern indexed; the arrows indicate diffraction spots due to the precipitate and the double arrow shows the central spot. The zone axis is $[\bar{1}12]_{FCC} // [111]_{P213}$. (d) DF image of the same area shown in (a), taken using the spot indexed as $[\bar{1}10]$.

that the PP crystallites spread not only along austenite and ferrite grain boundaries but are also present within the grains [23,24].

A low fraction of iron and manganese oxide is also present in the P6 sample, as revealed by the main reflection at $2\theta = 58.80^\circ$. We have identified it as FCC $Fe_{0.198}Mn_{0.802}O$ ICSD N° 60689 [45]. Although annealing is conducted under a protective Ar atmosphere, the high surface to volume ratio of ribbons facilitates their surface oxidation if the atmosphere is not completely pure.

4.3. Phase analysis

Firstly, we analysed if the typical X-ray reflections of the PP-phase, indicated in Section 4.2, correspond to any of the secondary phases found by other researchers in high-manganese steels, as previously summarized in Section 1. Table 4 explains why we discard the proposed phases in view of our X-ray results.

Taking a second approach, we see from Table 2 that this phase is richer in Mn, Ni, Cr and Si whereas its Fe content is lower with respect to the matrix, in agreement with the results of Maji et al. [46]. However, the amount of Si and Ni in the PP-phase, measured by TEM-EDS, is much lower than the relative atomic proportions corresponding to $Fe_5Ni_3Si_2$. According to these considerations and the previous results, we

proposed two hypotheses to identify the PP-phase. Following Maji et al. [46], one possibility is that the PP-phase crystallizes as a non-stoichiometric substitutional solid solution with the transition metals occupying the Ni and Si sites. The other possibility is that this phase is in fact a disordered solid solution of every alloy element in β -Mn, an allotropic form of Mn already found in other Fe–Mn based systems [47]. It coexists with γ and α -Fe at 700 °C but does not form at temperatures

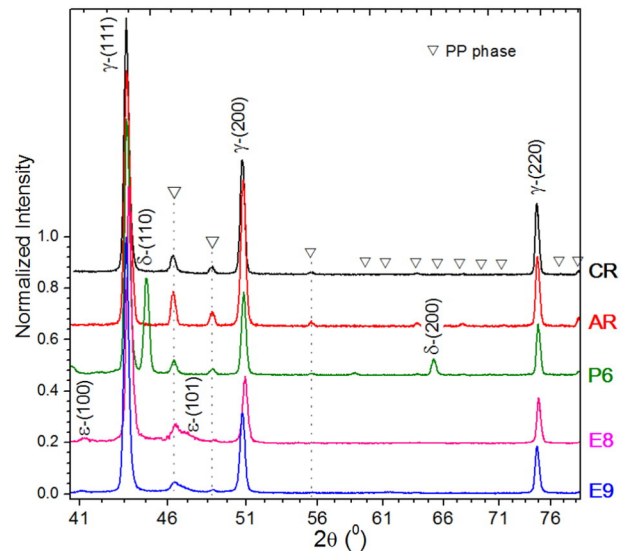


Fig. 3. X-ray patterns of the specimens with high concentration of the PP-phase, i.e. CR, AR, P6, E8 and E9 samples. Phases are identified as: γ : FCC austenite, δ : BCC ferrite, ϵ : HCP martensite, ∇ : PP-phase. Dotted vertical lines indicate the 2θ angles where the main prospective PP-phase reflections are found.

Table 2
TEM-EDS average composition (at. %) of four PP-phase particles found in E8 and P6 samples. The surrounding matrix composition is also given.

Sample	E8		P6	
	Particles	Matrix	Particles	Matrix
Fe	61.9	64.7	52.9	62.5
Mn	18.2	17.5	19.2	15.5
Cr	10.4	10.1	12.6	9.3
Ni	5.1	4.6	4.7	4.1
Si	5.2	3.3	10.6	8.6

Table 3
Crystallographic features of the phases present in the specimens under study, aside from the PP-phase.

Phases	Structure	Space group	a (nm)	c (nm)	Cell volume (nm ³)
γ -austenite	FCC	<i>Fm</i> 3 <i>m</i>	0.3615	–	0.4724
δ -ferrite	BCC	<i>Im</i> 3 <i>m</i>	0.2876	–	0.2379
ε -martensite	HCP	<i>P6</i> ₃ / <i>mmc</i>	0.2555	0.4145	0.2343

higher than 900 °C [48]. This is consistent with the absence of this phase's main reflections in the E10 sample.

The crystal structure of β -Mn is cubic, cP20, *P4*₁32 #213 [43], ICSD N° 642934 [45]. The atomic parameter equals 0.6314(5) nm and dissolves up to 32.9 at.% Fe and 16.7 at.% Si [48]. The crystallographic density is 7.20 g cm⁻³, whereas the atomic distribution within the unit cell is detailed in Table 5.

When we compare Cu K α X-ray patterns corresponding to β -Mn and τ -Fe₅Ni₃Si₂, it turns out that the diffraction reflections markedly coincide in 2θ positions, aside from the difference in cell parameter and (*hkl*) index at higher angles. However, the reflection intensities are not exactly the same due to: 1) the difference in atomic weight between Si and the metallic elements, and 2) the variation in the crystallographic symmetry of the atomic sites occupied. The substitutional atoms Cr, Mn, and Ni, as well as Fe, are all 3d transition metals and neighbours in the periodic table, so their scattering factors, which affect the relative intensities of the reflections, are quite similar. Moreover, both space groups correspond to the cubic system. However, *P2*₁3 has a lower Patterson symmetry (*Pm* $\bar{3}$) than *P4*₁32 (*Pm* $\bar{3}$ m). That is why at low 2θ angles, extra reflections are found for *P2*₁3 which do not satisfy the more restrictive (*hkl*) conditions of *P4*₁32. This is the case for the (200) reflection at $2\theta = 28.7^\circ$, which cannot be present if this phase space group were *P4*₁32, in view of the reflection condition for (*h00*): *h* must be equal to $4n$ (with *n* being an integer). Low-angle measurements are not typically performed in this alloy system since austenite, ferrite and ε -martensite reflections occur at angles above 35°. For that reason, we performed X-ray diffraction scans of the CR specimen from 22.5° to 34.5° with quite prolonged counting time per step, taking into consideration the weak intensity of low (*hkl*) peaks (see Fig. 5a). The angle range was selected so that two additional reflections located on both sides of the peak of interest were present: (111) at 24.85° and (210) at 32.26°. The diffractogram in Fig. 5a shows the presence of the (200) reflection, which supports our presumption: this intermetallic phase crystallizes as *P2*₁3, where Si atoms preferentially occupy distinct cell sites rather than

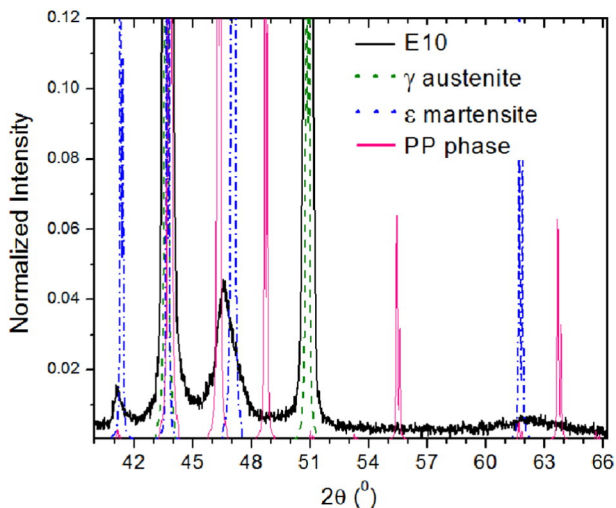


Fig. 4. Enlargement of the E10 X-ray pattern in the range of the most intense reflections of the PP-phase. Only γ -austenite and ε -martensite are present.

Table 4
Comparison of our experimental results against secondary phases reported in Fe–Mn–Si-based SMA.

Secondary phase	Discussion
$M_{23}C_6$ -type precipitates	Their structure is FCC, like $Cr_{23}C_6$ in [20] ICSD N° 62667 [45]. The PP-phase diffraction pattern in Fig. 3 does not correspond to a close packed cubic structure.
χ -phase (Fe _{1.01} Cr _{0.99})	The unit cell is tetragonal, <i>P4</i> ₂ / <i>mnm</i> S. G. (see ICSD N° 102747 [45]), and it forms when the Cr content is over 10 wt.%, which is not our case.
χ -phase (Fe ₁₈ Cr ₆ Mo ₅), where Mo is stoichiometrically substituted by transition metals.	The structure is BCC ICSD N° 102758 [45]. Also, it is a commonly recognized precipitate that forms in the ferrite/austenite phase boundary of duplex stainless steel alloys. Our X-ray measurements correspond to a lower symmetry cubic space group with a cell parameter smaller than the one determined by Stanford et al. [14], as we show in Table 7. These authors claim that the alloy phase constitution might significantly change after adding 1 wt.% Al, which is absent in the alloy under study.
α_1 Fe ₃ Si and β Mn ₃ Si intermetallic phases	Their structure is FCC: ICSD N° 56281 and ICSD N° 643647 [45], respectively. These phases can be found in the Fe–Mn–Si system under certain conditions different from the present work, as described in [48].

mixing randomly with the metallic elements. It must be mentioned that the peak at 31.1° is likely associated with tungsten from the filament that probably contaminates the Cu anode target due to X-ray tube ageing. It is noticeable owing to the extensive collecting time.

In view of these experimental results, we believe that the PP-phase is a 5:3:2 type intermetallic and this is how we will refer to it hereinafter.

In this scenario, we are able to index the X-ray reflections described in Section 4.2, which correspond to this 5:3:2 intermetallic (see Fig. 5b). The diffraction peak at $2\theta = 46.292^\circ$ results from the (301) planes being in the diffraction condition. Its relative intensity is 57%. Reflections at 48.694° and 55.433° are associated with the (311) and (312) planes, respectively. Their intensity is lower: 24% in the first case and 7% in the latter. Fig. 5b shows the full range X-ray pattern of the AR sample, where the Miller indexes are indicated for the reflections that can be observed in the pattern. The main reflection of the 5:3:2 intermetallic is located at 43.790° and arises when (221) lattice planes fulfil the Bragg condition. However, it overlaps with the strongest austenitic peak, so it can only be recognized by peak deconvolution in the refinement, as will be shown later.

Consequently, every Rietveld refinement was conducted considering that the 5:3:2 intermetallic structure is cubic with space group *P2*₁3. We estimate its chemical composition as Fe₄₈(Mn, Cr)₃₂(Ni, Si)₂₀, as our TEM-EDS results indicate (Table 2). Crystallographic features including atomic coordinates, symmetry and occupancy are listed in Table 6.

Our refinement results are summarized in Table 7 and Table 8. In Table 7, we identify and determine the weight percentage of each phase present in the sample. Also the lattice parameters and the crystallographic density are given. Table 8 shows the relevant refined parameters of specimens CR, AR, P6 and E9, which will be correlated with

Table 5
Atomic distribution within the cubic unit cell of β -Mn.

Atom	Wyckoff site	Site symmetry	x	y	z	Occ.	Cell formula units Z
Mn	8 c	.3.	0.06100	0.06100	0.06100	1.0	20
Mn	12 d	.2	1/8	0.20600	0.45600	1.0	

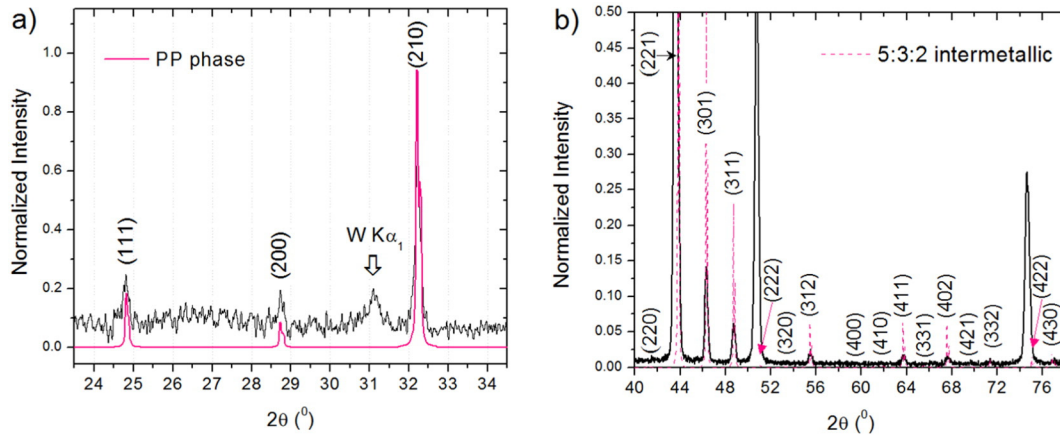


Fig. 5. (a) Low-angle X-ray measurement of the CR specimen showing the presence of the (200) reflection, which corresponds to the space group $P2_13$; (b) pattern of the 5:3:2 intermetallic phase showing the main reflections. Each reflection is labelled with the corresponding Miller indexes of $P2_13$ structure.

the microstructural and morphological properties described in Section 4.1. Values of $\langle D_{eff} \rangle$ represent the mean dimension of the coherently scattering crystals, thus the true grain size might be larger. However, the refinement becomes almost insensitive to crystallite size when it exceeds 200 nm [37]. It is worth mentioning that the goodness of fit is similar in all our Rietveld refinements. Therefore, the comparison between the refined parameters of all the specimens is straightforward.

Argumentation is due to the fact that we are including in the refinements microstructural defect parameters that in principle would not be necessary for our main purpose, which is the assessment of the crystal structure and actual presence of the 5:3:2 intermetallic phase. The analysis of the defect density and/or quality is only performed for refinement reliability. The 5:3:2 phase is a stable phase, whose presence is more or less independent of the thermomechanical processes applied to our current alloy. A single crystal, or even a single-phase polycrystal, of this phase is not currently available for crystallographic analysis and the current work tries to gather information from many distinctively treated samples to show the coherency of the proposition.

From Table 7, we see that the 5:3:2 intermetallic has an average lattice parameter equal to 0.6227(7) nm and a mean crystallographic density of 7.25(2) g cm⁻³. On the other hand, γ -austenite exhibits a cell parameter value of 0.3615(4) nm and a density of 7.49(3) g cm⁻³. The martensite c/a ratio equals 1.6, as expected considering its atomic arrangement corresponds to hexagonal close packing.

The identified phases have approximately the same density, so the volume percentage is similar to the weight percentage reported in Table 7.

The ingots, originally austenitic, were conventionally and asymmetrically hot-rolled at the same temperature and reduction step conditions, and finally annealed at 650 °C for 30 min. We believe that the same final annealing temperature is the reason why the amount of 5:3:2 intermetallic is similar in both CR and AR specimens, independently of the kind of stress involved in each thermomechanical treatment. A combination of high-intensity stress fields (shear and normal) acts on the

material during asymmetric rolling. Hence, the microstrain and the ensuing dislocation density in the austenitic matrix are one order of magnitude higher with respect to the refined values corresponding to the CR specimen. A similar relative increase is observed in the compound fault probability of the austenite. This coincides with the OM micrograph shown in Fig. 1a. Among the rolled specimens, the smallest intermetallic crystallographic domains are found in the AR specimen. Moreover, the accumulated microstrain in the 5:3:2 phase is at least four orders of magnitude higher in comparison to the CR case. This suggests that dislocations massively develop and interact within the intermetallic grains during annealing at 650 °C. Thus, it is likely that they subdivide the original grains into smaller crystalline domains.

As was explained above, the current alloy contains elements that stabilize δ -ferrite and γ -austenite, simultaneously (see Table 2). During melt-spinning, the rapid solidification can stabilize the high-temperature ferritic phase, as stated by Druker et al. [23]. The ribbons were completely ferritic in the as cast condition. In sample P6, during annealing at 600 °C for 60 min, 71 wt.% of the δ -phase transforms to γ , while the amount of secondary precipitates increases up to 11 wt.%. Austenite and 5:3:2 phase crystallite sizes are smaller than in CR and AR samples, which is reasonable because grain refinement is produced by the rapid solidification technique itself. The dislocation density is in the order of 1×10^{10} cm⁻² in austenite and 1×10^9 cm⁻² in ferrite, and could be originated by the local stresses associated to the precipitation of the 5:3:2 intermetallic. TEM images of another as cast ribbon specimen where γ - and δ -phases coexist, confirmed the presence of 5:3:2 intermetallic and dislocation arrays, even without annealing at intermediate temperatures [23]. Apparently, nucleation and growth of this coherent phase enhances the development of defects in the material.

Table 6

Atomic distribution and cell site occupation within the cubic unit cell of intermetallic 5:3:2 phase (formerly referred as the PP-phase).

Atom	Wyckoff site	Site symmetry	x	y	z	Occupancy
Cr	4 a	.3.	0.689	0.689	0.689	0.5
Ni	4 a	.3.	0.689	0.689	0.689	0.5
Fe	12 b	1	0.794	0.956	0.375	0.8
Mn	12 b	1	0.794	0.956	0.375	0.2
Si	4 a	.3.	0.061	0.061	0.061	0.5
Mn	4 a	.3.	0.061	0.061	0.061	0.35
Cr	4 a	.3.	0.061	0.061	0.061	0.15

Table 7

Identification, relative weight percentage, crystallographic lattice parameters, and density of the phases present in CR, AR, P6, E8 and E9 specimens.

Sample	Phases	wt.%	a (nm)	c (nm)	δ_{XRD} (g cm ⁻³)
CR	γ -austenite	88	0.3617		7.48
	5:3:2 intermetallic	12	0.6228		7.25
AR	γ -austenite	82	0.3619		7.46
	5:3:2 intermetallic	18	0.6235		7.22
P6	γ -austenite	71	0.3608		7.53
	δ -ferrite	13	0.2876		7.43
	5:3:2 intermetallic	11	0.6218		7.28
E8	Fe _{0.198} Mn _{0.802} O	5	0.4466		5.30
	γ -austenite	77	0.3616		7.48
	ϵ -martensite	15	0.2556	0.4124	7.58
E9	5:3:2 intermetallic	8	0.6233		7.23
	γ -austenite	82	0.3616		7.48
E9	ϵ -martensite	14	0.2556	0.4159	7.52
	5:3:2 intermetallic	4	0.6222		7.26

Table 8
Microstructural refined results corresponding to the phases present in CR, AR, P6 and E9 specimens.

Sample	Phases	Crystallite size <D _{eff} > (nm)	r.m.s microstrain (<ε _{hh} ² > ^{1/2})	Compound fault probability [1.5(α' + α'') + β]	Dislocation density ρ _{av.} (cm ⁻²)	GoF
CR	γ	180	4 × 10 ⁻⁴	1 × 10 ⁻⁵	4 × 10 ⁹	1.3
	5:3:2 intermet.	160	1 × 10 ⁻⁹			
AR	γ	190	2 × 10 ⁻³	5 × 10 ⁻⁴	3 × 10 ¹⁰	1.4
	5:3:2 intermet.	80	7 × 10 ⁻⁵			
P6	γ	160	8 × 10 ⁻⁴	6 × 10 ⁻⁶	1 × 10 ¹⁰	1.4
	δ	80	1 × 10 ⁻⁴		4 × 10 ⁹	
	5:3:2 intermet.	60	1 × 10 ⁻⁴			
	oxide	20				
E9	γ	160	4 × 10 ⁻⁷	4 × 10 ⁻³	6 × 10 ⁶	1.3
	ε	7	1 × 10 ⁻⁵			
	5:3:2 intermet.	80	1 × 10 ⁻⁵			

Finally, the ECAP samples contain the lowest weight percentage of the 5:3:2 intermetallic phase. The prestrained material was annealed at 800, 900 and 1000 °C for 30 min, and then compressed to a strain of 3.8%. The specimen annealed at 800 °C has 8 wt.% of the intermetallic phase, while the sample annealed at 900 °C contains 4 wt.%. It seems that temperatures close to 800 °C are more favourable than those around 900 °C for the precipitation mechanisms, leading to a higher proportion of the 5:3:2 intermetallic. This influence of temperature on the formation of the intermetallic was corroborated by annealing at 1000 °C, since no trace of the phase can be found in the E10 specimen. Apparently, the 5:3:2 phase decomposes and its constituting elements dissolve into the austenitic matrix at 1000 °C. The crystallite size of γ is somewhat smaller than in CR and AR specimens, and the grain size of 5:3:2 intermetallic is similar as in the rest of the samples, with the exception of the CR case where larger crystallites develop. ε-martensite crystallites are noticeably small, in accordance with the typical martensitic plate morphology. Our results suggest that the elastic strain fields are negligible, though a significant density of stacking faults can be found in γ, as expected in this shape memory alloy with low stacking fault energy. Fig. 6 shows the Maud output graphic corresponding to the E9 specimen; each phase is represented in a different colour. The quality of the refinement can be observed.

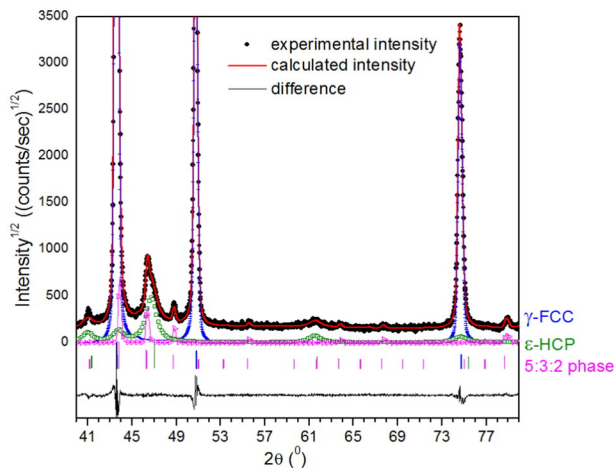


Fig. 6. Rietveld refinement output graphic from the specimen E9. Reflections from each phase are represented in different colours: γ-FCC (blue), ε-HCP (green) and 5:3:2 intermetallic (pink). In the upper part: X-ray measurement superimposed over the refinement fitted curve; in the middle part: vertical bars representing the 2θ reflections of each phase; in the lower part: differences between the experimental pattern and the calculated profile using Maud.

5. Conclusions

In this work samples of an Fe–15Mn–5Si–9Cr–5Ni wt.% (nominal composition) SMA, processed by different methods, were studied in order to analyse the phases present in each case. A certain amount of second-phase precipitates were produced during the applied procedures. The alloy's crystallographic structure and properties have been discussed by several authors in the field of high-manganese ferrous alloys. We arrived at the following conclusions:

An intermetallic phase is found in all the samples. The nucleation and growth mechanisms seem independent of the thermomechanical treatment and/or the preparation method. This was the case whether processing was by conventional or asymmetric rolling, equal-channel angular pressing followed by annealing at different temperatures and then compression to activate the martensitic transformation, or melt-spinning. The formation of the new phase occurs during recovery annealing over an intermediate temperature range between 600 and 900 °C.

From our X-ray analysis, the precipitated phase is a cubic Fe₅Ni₃Si₂ type intermetallic of the space group *P2₁3*, i.e. it is isostructural to the π-phase Cr₃Ni₅Si₂. Therefore, Si atoms occupy distinct cell sites rather than being randomly mixed with the metallic elements. The average lattice parameter equals 0.623 nm and the mean crystallographic density is 7.2 g/cm, according to our results refined by the Rietveld method using the Maud software. In addition, TEM-EDS measurements in different samples indicate that the mean chemical composition of this new phase is Fe₄₈(Mn, Cr)₃₂(Ni, Si)₂₀.

This Fe–15Mn–5Si–9Cr–5Ni SMA has also been analysed by synchrotron measurements. The results are in agreement with the conclusions of this work and will be reported in the future.

Acknowledgements

The authors wish to thank Dr. M. Stout for proofreading this manuscript. Financial support from the Agencia Nacional de Promoción Científica y Tecnológica ANPCyT (grant number PICT 1341-2011) is kindly acknowledged.

References

- [1] K. Otsuka, A. Saxena, J. Deng, X. Ren, Mechanism of the shape memory effect in martensitic alloys: an assessment, *Philos. Mag.* 91 (2011) 4514–4535, <http://dx.doi.org/10.1080/14786435.2011.608735>.
- [2] A. Sato, E. Chishima, K. Soma, T. Mori, Shape memory effect in g-e transformation in Fe–30Mn–1Si alloy single crystals, *Acta Metall.* 30 (1982) 1177–1183, [http://dx.doi.org/10.1016/0001-6160\(82\)90011-6](http://dx.doi.org/10.1016/0001-6160(82)90011-6).
- [3] A. Druker, A. Baruj, J. Malarría, Effect of rolling conditions on the structure and shape memory properties of Fe–Mn–Si alloys, *Mater. Charact.* 61 (2010) 603–612, <http://dx.doi.org/10.1016/j.matchar.2010.03.005>.
- [4] N. Stanford, D.P. Dunne, H. Li, Re-examination of the effect of NbC precipitation on shape memory in Fe–Mn–Si-based alloys, *Scr. Mater.* 58 (2008) 583–586, <http://dx.doi.org/10.1016/j.scriptamat.2007.11.018>.

- [5] O. Söderberg, X.W. Liu, P.G. Yakovenko, K. Ullakko, V.K. Lindroos, Corrosion behaviour of Fe–Mn–Si based shape memory steels trained by cold rolling, *Mater. Sci. Eng. A* 273–275 (1999) 543–548, [http://dx.doi.org/10.1016/S0921-5093\(99\)00396-2](http://dx.doi.org/10.1016/S0921-5093(99)00396-2).
- [6] A. Baruj, H.E. Troiani, The effect of pre-rolling Fe–Mn–Si-based shape memory alloys: mechanical properties and transmission electron microscopy examination, *Mater. Sci. Eng. A* 481–482 (2008) 574–577, <http://dx.doi.org/10.1016/j.msea.2007.02.140>.
- [7] M. Sade, A. Baruj, H.E. Troiani, FCC/HCP Martensitic Transformation Temperatures and Thermal Cycling Evolution in Fe–Mn–Cr Alloys, *New Dev Metall Appl High Strength Steels Buenos Aires 2008*, Vol. 1 Vol. 2, Wiley-VCH Verlag GmbH & Co 2008, p. 87339.
- [8] H. Otsuka, H. Yamada, T. Maruyama, H. Tanahashi, S. Matsuda, M. Murakami, Effects of alloying additions on Fe–Mn–Si shape memory alloys, *ISIJ Int.* 30 (1990) 674–679, <http://dx.doi.org/10.2355/isijinternational.30.674>.
- [9] H. Otsuka, H. Yamada, H. Tanahashi, T. Maruyama, Shape memory effect in Fe–Mn–Si–Cr–Ni polycrystalline alloys, *Mater. Sci. Forum* 56–58 (1990) 655–660 doi: 10.4028/www.scientific.net/MSF.56-58.655.
- [10] H. Peng, Y. Wen, Y. Du, J. Chen, Q. Yang, A new set of Creq and Nieq equations for predicting solidification modes of cast austenitic Fe–Mn–Si–Cr–Ni shape memory alloys, *Metall. Mater. Trans. B Process Metall. Mater. Process. Sci.* 45 (2014) 6–11, <http://dx.doi.org/10.1007/s11663-013-0005-8>.
- [11] H. Peng, Y. Wen, Y. Du, Q. Yu, Q. Yang, Effect of manganese on microstructures and solidification modes of cast Fe–Mn–Si–Cr–Ni shape memory alloys, *Metall. Mater. Trans. B* 44 (2013) 1137–1143 <http://dx.doi.org/10.1007/s11663-013-9880-2>.
- [12] H.C. Lin, C.S. Lin, K.M. Lin, Y.C. Chuang, An investigation of grain-boundary phase in Fe–30Mn–6Si–5Cr shape memory alloy, *J. Alloys Compd.* 319 (2001) 283–289, [http://dx.doi.org/10.1016/S0925-8388\(01\)00905-7](http://dx.doi.org/10.1016/S0925-8388(01)00905-7).
- [13] B.C. Maji, M. Krishnan, The effect of microstructure on the shape recovery of a Fe–Mn–Si–Cr–Ni stainless steel shape memory alloy, *Scr. Mater.* 48 (2003) 71–77, [http://dx.doi.org/10.1016/S1359-6462\(02\)00348-2](http://dx.doi.org/10.1016/S1359-6462(02)00348-2).
- [14] N. Stanford, D.P. Dunne, B.J. Monaghan, Austenite stability in Fe–Mn–Si-based shape memory alloys, *J. Alloys Compd.* 430 (2007) 107–115, <http://dx.doi.org/10.1016/j.jallcom.2006.04.054>.
- [15] N.E. Stanford, K. Chen, D.P. Dunne, X. Jin, Effect of alloying additions on the SFE, neél temperature and shape memory effect in Fe–Mn–Si-based alloys, *ISIJ Int.* 47 (2007) 883–889, <http://dx.doi.org/10.2355/isijinternational.47.883>.
- [16] T. Kirindi, M. Dikici, Microstructural analysis of thermally induced and deformation induced martensitic transformations in Fe–12.5 wt.% Mn–5.5 wt.% Si–9 wt.% Cr–3.5 wt.% Ni alloy, *J. Alloys Compd.* 407 (2006) 157–162, <http://dx.doi.org/10.1016/j.jallcom.2005.06.023>.
- [17] T. Kirindi, E. Güler, M. Dikici, Effects of homogenization time on the both martensitic transformations and mechanical properties of Fe–Mn–Si–Cr–Ni shape memory alloy, *J. Alloys Compd.* 433 (2007) 202–206, <http://dx.doi.org/10.1016/j.jallcom.2006.06.091>.
- [18] Y.H. Wen, H.B. Peng, P.P. Sun, G. Liu, N. Li, A novel training-free cast Fe–18Mn–5.5Si–9.5Cr–4Ni shape memory alloy with lathy delta ferrite, *Scr. Mater.* 62 (2010) 55–58, <http://dx.doi.org/10.1016/j.scriptamat.2009.10.004>.
- [19] E. Folkhard, *Welding Metallurgy of Stainless Steels*, Springer-Verlag, Wein, 1988 <http://dx.doi.org/10.1007/978-3-7091-8965-8>.
- [20] D. Bu, H. Peng, Y. Wen, N. Li, Influence of ageing on wear resistance of an Fe–Mn–Si–Cr–Ni–Ti–C shape memory alloy, *Mater. Des.* 32 (2011) 2969–2973, <http://dx.doi.org/10.1016/j.matdes.2011.01.032>.
- [21] K.-M. Lin, J.-H. Chen, C.-C. Lin, C.-H. Liu, H.-C. Lin, Optimization of shape-memory effect in Fe–Mn–Si–Cr–Re shape-memory alloys, *J. Mater. Eng. Perform.* 23 (2014) 2327–2332, <http://dx.doi.org/10.1007/s11665-014-1071-z>.
- [22] C.H. Yang, H.C. Lin, K.M. Lin, H.K. Tsai, Effects of thermo-mechanical treatment on a Fe–30Mn–6Si shape memory alloy, *Mater. Sci. Eng. A* 497 (2008) 445–450, <http://dx.doi.org/10.1016/j.msea.2008.07.057>.
- [23] A. Druker, P. La Roca, P. Vermaut, P. Ochin, J. Malarría, Microstructure and shape memory properties of Fe–15Mn–5Si–9Cr–5Ni melt-spun ribbons, *Mater. Sci. Eng. A* 556 (2012) 936–945, <http://dx.doi.org/10.1016/j.msea.2012.07.097>.
- [24] A.V. Druker, A. Perotti, I. Esquivel, J. Malarría, A manufacturing process for shaft and pipe couplings of Fe–Mn–Si–Ni–Cr shape memory alloys, *Mater. Des.* 56 (2014) 878–888, <http://dx.doi.org/10.1016/j.matdes.2013.11.032>.
- [25] A.V. Druker, V. Fuster, L. Isola, R. Bolmaro, J. Malarría, Effect of the manufacturing process on the texture and the fraction of stress-induced martensite in an Fe–Mn–Si–Cr–Ni shape memory alloy, *Procedia Mater. Sci.* 9 (2015) 187–194, <http://dx.doi.org/10.1016/j.mspro.2015.04.024>.
- [26] D.L. Kaiser, J.R.L. Watters, *Standard Reference Material®660b*, 2010 1–5.
- [27] H.M. Rietveld, A profile refinement method for nuclear and magnetic structures, *J. Appl. Crystallogr.* 2 (1969) 65–71, <http://dx.doi.org/10.1107/S0021889869006558>.
- [28] L. Lutterotti, S. Matthies, H.-R. Wenk, Combined texture and structure analysis of deformed limestone from time-of-flight neutron diffraction spectra, *J. Appl. Phys.* 81 (1997) 594–600, <http://dx.doi.org/10.1063/1.364220>.
- [29] L. Lutterotti, Maud (Material Analysis Using Diffraction), 1997 <http://maud.radiographema.com> accessed May 1, 2015.
- [30] L. Lutterotti, P. Scardi, Simultaneous structure and size–strain refinement by the Rietveld method, *J. Appl. Crystallogr.* 23 (1990) 246–252, <http://dx.doi.org/10.1107/S0021889890002382>.
- [31] L. Lutterotti, S. Gialanella, R. Caudron, Diffraction methods for the characterisation of defects in intermetallic compounds, *Mater. Sci. Forum* 228–231 (1996) 551–556 doi:10.4028/www.scientific.net/MSF.228-231.551.
- [32] S. Matthies, L. Lutterotti, H.R. Wenk, Advances in texture analysis from diffraction spectra, *J. Appl. Crystallogr.* 30 (1997) 31–42, <http://dx.doi.org/10.1107/S0021889896006851>.
- [33] I. Lonardelli, H.R. Wenk, L. Lutterotti, M. Goodwin, Texture analysis from synchrotron diffraction images with the Rietveld method: dinosaur tendon and salmon scale, *J. Synchrotron Radiat.* 12 (2005) 354–360, <http://dx.doi.org/10.1107/S090904950500138X>.
- [34] R.A. Young, *The Rietveld Method*, Oxford University Press Inc., New York, 1993.
- [35] A. Druker, C. Sobrero, H.-G. Brokmeier, J. Malarría, R. Bolmaro, Texture evolution during thermomechanical treatments in Fe–Mn–Si shape memory alloys, *Mater. Sci. Eng. A* 481–482 (2008) 578–581, <http://dx.doi.org/10.1016/j.msea.2006.10.214>.
- [36] U.F. Kocks, C.N. Tomé, H.–P. Wenk, *Texture and Anisotropy Preferred Orientations in Polycrystals and Their Effect on Materials Properties*, 1st ed. Cambridge: Cambridge University Press, 1998.
- [37] L. Lutterotti, R. Vasin, H.-R. Wenk, Rietveld texture analysis from synchrotron diffraction images. I. Calibration and basic analysis, *Powder Diffraction* 29 (2014) 76–84, <http://dx.doi.org/10.1017/S0885715613001346>.
- [38] N.C. Popa, The (hkl) dependence of diffraction-line broadening caused by strain and size for all Laue groups in Rietveld refinement, *J. Appl. Crystallogr.* 31 (1998) 176–180 <http://dx.doi.org/10.1107/S0021889897009795>.
- [39] B.E. Warren, *X-Ray Diffraction*.pdf. Massachusetts, Addison-Wesley Publishing Company Inc, 1969.
- [40] G.K. Williamson, R.E. Smallman III, Dislocation densities in some annealed and cold-worked metals from measurements on the X-ray Debye–Scherrer spectrum, *Philos. Mag.* 1 (1956) 34–46, <http://dx.doi.org/10.1080/14786435608238074>.
- [41] M.S. Paterson, X-ray diffraction by face-centered cubic crystals with deformation faults, *J. Appl. Phys.* 23 (1952) 805–811, <http://dx.doi.org/10.1063/1.1702312>.
- [42] *Monographs in Practical Electron Microscopy in Materials Science*, Van Nostrand Reinhold Co., Hemden, V.A., 1976
- [43] T. Hahn (Ed.), *International Tables for Crystallography Volume A: Space-group symmetry*, 5th ed. Springer, Netherlands, 2002 <http://dx.doi.org/10.1107/97809553602060000100>.
- [44] S. Ackerbauer, N. Krendelsberger, F. Weitzer, K. Hiebl, J.C. Schuster, The constitution of the ternary system Fe–Ni–Si, *Intermetallics* 17 (2009) 414–420, <http://dx.doi.org/10.1016/j.intermet.2008.11.016>.
- [45] FIZ Karlsruhe Inorganic Crystal Structure Database ICSD, Release 2011–2, 1998 <https://icsd.fiz-karlsruhe.de>.
- [46] B.C. Maji, M. Krishnan, V.V. Rama Rao, The microstructure of an Fe–Mn–Si–Cr–Ni stainless steel shape memory alloy, *Metall. Mater. Trans. A* 34 (2003) 1029–1042, <http://dx.doi.org/10.1007/s11661-003-0124-y>.
- [47] R. Umino, X.J. Liu, Y. Sutou, C.P. Wang, I. Ohnuma, R. Kainuma, Experimental determination and thermodynamic calculation of phase equilibria in the Fe–Mn–Al system, *J. Phase Equilib. Diffus.* 27 (2006) 54–62, <http://dx.doi.org/10.1361/105497106X92817>.
- [48] G. Effenberg, S. Ilyenko, (Pierre Perrot). Iron–manganese–oxygen, *Iron Syst Part 4*, 11D4 2008, pp. 235–261, <http://dx.doi.org/10.1007/978-3-540-78644-3>.